Nano Research
2019, 12(1): 91–99

ISSN 1998-0124 CN 11-5974/O4
https://doi.org/10.1007/s12274-018-2185-7

Research Article

Orientation-controlled, low-temperature plasma growth and applications of h-BN nanosheets

Ivan Sergeevich Merenkov[1,2] (✉), Mikhail Sergeevich Myshenkov[3], Yuri Mikhailovich Zhukov[3], Yohei Sato[4], Tatyana Sergeevna Frolova[5,6,7], Denis Vasilevich Danilov[3], Igor Alekseevich Kasatkin[3], Oleg Sergeevich Medvedev[3], Roman Vladimirovich Pushkarev[1], Olga Ivanovna Sinitsyna[5,7], Masami Terauchi[4], Irina Alekseevna Zvereva[3], Marina Leonidovna Kosinova[1], and Ken Ostrikov[8,9]

[1] *Nikolaev Institute of Inorganic Chemistry SB RAS, Novosibirsk 630090, Russia*
[2] *Ural Federal University, Ekaterinburg 620002, Russia*
[3] *Saint-Petersburg State University, St. Petersburg 199034, Russia*
[4] *IMRAM, Tohoku University, Sendai 980-8577, Japan*
[5] *Institute of Cytology and Genetics SB RAS, Novosibirsk 630090, Russia*
[6] *Vorozhtsov Novosibirsk Institute of Organic Chemistry SB RAS, Novosibirsk 630090, Russia*
[7] *Novosibirsk State University, Novosibirsk 630090, Russia*
[8] *School of Physics, Chemistry and Mechanical Engineering, Queensland University of Technology, Brisbane QLD 4000, Australia*
[9] *CSIRO-QUT Joint Sustainable Processes and Devices Laboratory, P.O. Box 218, Lindfield NSW 2070, Australia*

Received: 6 July 2018 / **Revised:** 20 August 2018 / **Accepted:** 20 August 2018

ABSTRACT

Dimensionality and orientation of hexagonal boron nitride (h-BN) nanosheets are promising to create and control their unique properties for diverse applications. However, low-temperature deposition of vertically oriented h-BN nanosheets is a significant challenge. Here we report on the low-temperature plasma synthesis of maze-like h-BN nanowalls (BNNWs) from a mixture of triethylamine borane (TEAB) and ammonia at temperatures as low as 400 °C. The maze-like BNNWs contained vertically aligned stacks of h-BN nanosheets. Wavy h-BN nanowalls with randomly oriented nanocrystalline structure are also fabricated. Simple and effective control of morphological type of BNNWs by the deposition temperature is demonstrated. Despite the lower synthesis temperature, thermal stability and oxidation resistivity of the maze-like BNNWs are higher than for the wavy nanowalls. The structure and oxidation of the nanowalls was found to be the critical factor for their thermal stability and controlled luminescence properties. Cytotoxic study demonstrated significant antibacterial effect of both maze-like and wavy h-BN nanowalls against *E. coli*. The reported results reveal a significant potential of h-BN nanowalls for a broad range of applications from electronics to biomedicine.

KEYWORDS

boron nitride nanosheets, nanowalls, chemical vapor deposition, cytotoxicity, light emission, thermal stability

1 Introduction

Two-dimensional (2D) nanostructures have been at the forefront of materials science after the discovery of graphene [1] and other single-layered materials such as hexagonal boron nitride (h-BN) [2]. In particular, h-BN nanosheets are well-known for outstanding thermal conductivity and electronic properties [2], in addition to excellent mechanical strength [3], chemical inertness [4], and distinctive deep UV luminescence [5, 6]. These and many other properties make pristine and functionalized h-BN nanosheets highly-promising for diverse applications in biomedical, electronic, composite, environmental and sustainable energy-related fields [7–13]. Many of these applications rely on the structural and morphological properties determined by the dimensionality and orientation of the structures.

However, the presently available options to control h-BN properties in applications by the dimensionality and orientation are much less explored and utilized as compared to similar carbon nanostructures, even though h-BN is an isostructural analog of carbon. Indeed, a very large number of publications report on graphene sheets with different orientations, from horizontal to normally oriented and mixed structures [14]. This morphological flexibility combined with graphitic structure, reactive edges and some other properties of oriented graphene sheets make them ideal for applications in electrochemical capacitors, electron emitting, environmental and bio-sensing devices [15–20].

In contrast, only a limited number of reports on the synthesis of vertically oriented h-BN nanosheets (h-BN nanowalls (BNNWs)) have been published so far [21–23], in part because of the complex precursors and synthesis procedures commonly requiring high temperatures. For example, BNNWs can be formed from $BF_3 + N_2 + H_2$ or even more complex $BCl_3 + NH_3 + N_2 + H_2$ or B + MgO + FeO + NH_3 reactive gas mixtures at process temperatures 800–1,300 °C [21–23]. Such high process temperatures make it impossible to produce h-BN nanowalls on thermal-sensitive substrates without transfer. The types of morphologies reported so far are mostly limited to a few basic configurations such as petal-like and wavy morphologies. However, the ordering of such structures over the surface is typically

Address correspondence to merenkov@niic.nsc.ru

less regular compared to carbon counterparts. Moreover, regular patterns of maze-like BNNWs with vertically oriented structure, so common for carbon nanowalls, have not been synthesized so far.

The intrinsic difficulty on the way to reliable low-temperature synthesis of h-BN is to a large extent related to the high thermodynamic stability of the boron-containing precursors such as boron halides. One potential solution is to use organoboron compounds, such as borazine and amine-boranes, as chemical vapor deposition (CVD) precursors. However, low-temperature decomposition of organoborons suffers from large amorphous boron nitride and carbonitride deposits [24, 25] and requires additional low-temperature crystallization mechanisms.

Here we use low-temperature thermally non-equilibrium plasma which helps simultaneously decompose precursors and crystallize the oriented and ordered structures at low temperatures. These features of plasma have been demonstrated for a large number of organic and inorganic materials [26, 27]. High rates of reforming of organoboron compounds make the plasma process much safer compared to thermal processing of boron halides which requires sophisticated safety procedures as well as corrosion-resistant reactors. However, high rates of precursor decomposition in plasma often lead to chaotically oriented BN nanosheets with a mixed amorphous and nanocrystalline structure, and the process temperatures still remain high (~ 700 °C) [28, 29].

Previous studies suggest that the use of various toxic precursors potentially limits the utility of h-BN nanosheets in biomedical products and devices. This issue is particularly critical for low-temperature processes where incomplete decomposition of such precursors may leave toxic residues in the nanosheets. This is one of the reasons of the many contradictory reports on biocompatibility and in particular, cytotoxicity of h-BN nanosheets and other BN structures such as nanotubes [8, 30]. Moreover, to the best of our knowledge, cytotoxicity of h-BN nanowall-like structures has not been investigated so far.

This work fills the above knowledge gaps and reports on the low-temperature, plasma enabled synthesis of the previously unknown regular patterns of maze-like vertically oriented h-BN nanowalls from triethylamine borane (TEAB) and ammonia precursors at temperatures as low as 400 °C. Simple variation of the process temperature makes it possible to produce different morphological types of h-BN such as also relatively uncommon patterns of wavy structures. Systematic studies of structural, luminescent and cytotoxic properties of morphologically different h-BN nanostructures reveal a significant potential of our simple and robust approach for the production of diverse oriented h-BN nanostructures for a broad range of applications from electronics to biomedicine.

2 Methods

2.1 h-BN nanowalls synthesis

The h-BN nanowalls were synthesized by plasma enhanced chemical vapor deposition (PECVD) from a gas mixture of TEAB ($(C_2H_5)_3N{\cdot}BH_3$) and ammonia in ratio 1:1. More details on the synthesis facility can be find elsewhere [31]. Si(100) were used as substrates. The deposition was performed at the temperatures 400–600 and 700 °C, with the plasma power at 20 W.

2.2 Material characterization

The elemental composition was determined by X-ray photoelectron spectroscopy (XPS; Thermo Fisher Scientific Escalab 250Xi). The sample surface was not previously treated by Ar^+ ion bombardment. The transmission electron microscopy (TEM) observation and electron energy loss spectroscopy (EELS) measurements of the BNNWs were conducted by a JEM-2010 and a JEM-2010FEF equipped with a monochromator operated at 100 kV [32]. The energy-resolution of the EELS spectra was 80 meV–0.15 eV. The nanowalls morphology was studied using Zeiss Merlin scanning electronic microscope. The diffraction data were obtained with the Bruker D8 Discover high-resolution diffractometer in an asymmetric mode with the grazing angle ω = 2° using CuKα radiation (λ = 0.154184 nm). The data were processed with the TOPAS 4.2 software. The cathodoluminescence spectra in the wavelength range from 200 to 800 nm were obtained using the Zeiss Supra 40VP electron microscope equipped with the Gatan MonoCL3+ system for cathodoluminescence registration.

2.3 Thermal annealing

The visual thermal analysis was performed using the Carl-Zeiss AxioScope A1 optical microscope and the Linkam TS1500 stage within the temperature range from room temperature to 1,000 °C. The Netzsch STA 449 F3 Jupiter ASC Simultaneous Thermal Analyzer was used for thermal annealing of samples in the gaseous atmospheres of Ar (< 0.01% O_2) and dry air at 1,100 °C during 10 min. Heating at 10 °C/min was followed by cooling at 40 °C/min.

2.4 Antibacterial test

The cytotoxic activity of nanowalls was investigated by antibacterial drop-test against *E. coli* PQ37 strain (F. Quillardet, France) as Gram-negative model. Before each microbiological experiment, all the samples were sterilized with 70% ethanol and dried under UV. The *E. coli* overnight culture were cultured on a nutrient LB medium at 37 °C for 24 h. Then, 100 μL of the cultured bacteria was spread on a surface of test samples within an area of 1 cm × 1 cm. After incubation of the sample for 60 min at room temperature, the bacteria were washed from the surface of the sample with 3 mL of phosphate buffered saline (PBS) in the sterilized Petri dish and diluted 6-fold by PBS. Then, 100 μL of the bacterial suspension was spread on a LB agar plate and incubated at 37 °C for 24 h to count the surviving bacterial colonies. The total number of the cells forming unit was determined by area based estimation. Antimicrobial test was carried out independently three times with three repeats in the experiment for each sample. The result is presented as the mean value ± standard error of the mean.

3 Results and discussion

3.1 Morphological features

Figure 1 shows scanning electron microscopy (SEM) images ((a)–(d)) and schematics ((e) and (f)) of the two morphological types of h-BN nanowalls grown for 120 min. The first type of nanowalls was deposited in the temperature range of 400–600 °C. This type of h-BNNWs was named "maze-like". The surface and the cross-section SEM images (Figs. 1(a) and 1(c)) demonstrate the well-separated platelets with bending morphology positioned vertically with respect to the substrate surface. The length and thickness of the nanowalls were in the range of 50–250 and 10–25 nm, respectively. On the other hand, the synthesis temperature of the second type of BNNWs was 700 °C. They contained highly bent and crumpled platelets with the thickness in the range of 10–20 nm. This type of h-BN nanowalls was named "wavy". The cross-section SEM image in Fig. 1(d) shows the principal differences between the maze-like and the wavy nanowalls. The platelets in the wavy nanowalls had chaotic orientation and could start growing at any point in the sample, whereas the nucleation points of the maze-like nanowalls were located at the substrate surface. In addition, only vertical channels were detected for the maze-like BNNWs, and only pores without specific direction—in wavy BNNWs. The synthesis temperature of 400 °C was much lower than that earlier reported for the fabrication of h-BN nanowalls by both chemical [21–23] and physical vapor deposition [33]. Moreover, synthesis of two morphological types of nanowalls

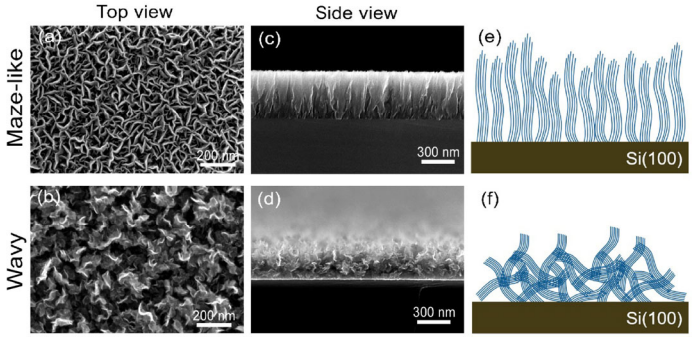

Figure 1 New plasma process produced two distinctive types of h-BN nanowall structures, imaged by SEM: (a) and (b) top view and (c) and (d) side view of maze-like and wavy h-BN nanowalls. (a) and (c) The maze-like BNNWs with regular morphology pattern and vertically oriented structure were synthesized at the minimal known temperature—400 °C. In contrast, (b) and (d) the wavy BNNWs have chaotically oriented structure. Schematics showing the difference between the stacking of (e) maze-like and (f) wavy h-BN nanowalls. The deposition temperature controlled switching of morphology makes it possible to vary the nanowall properties such as surface area and antibacterial activity.

in one process has only been previously reported for carbon nanowalls, which changed their morphology depending on the deposition time [34] and inclination of substrate [35].

3.2 Bonding states and elemental composition

In order to determine elemental compositions of h-BN nanowalls, XPS analyses were performed. The survey XPS spectra (Fig. S1 in the Electronic Supplementary Material (ESM)) showed the presence of carbon, oxygen and fluorine atoms on the surface in addition to the main elements—boron and nitrogen. The F1s photoemission peak corresponds to fluohydrocarbon impurity on the surface due to the use of PTFE packing, while O1s and C1s appear due to both surface contamination and doping defects possibly because of considerable reactivity between B and O or C atoms.

The deconvoluted high-resolution C1s, B1s and N1s XPS spectra of the maze-like and wavy h-BN nanowalls (Fig. 2) displayed some levels of asymmetry and broadening which suggest the existence of more than one type of bonding scheme for the atoms [36]. The B1s spectra can be fitted by three curves with binding energy peaks at 190.8, 191.8, and 189.5 eV. The main peak centered at 190.8 eV was attributed to the boron atoms surrounded by three nitrogen atoms as in the structure of h-BN [37]. The peaks centered at 191.8 and 189.5 eV can be assigned to boron atoms simultaneously bonded with nitrogen and oxygen (N–B–O) [38] or carbon (N–B–C) [39], respectively. The density of carbon-containing bonds was higher in wavy nanowalls, possibly due to deeper decomposition of the precursor at high synthesis temperature.

The C1s spectra in Fig. 2(b) were well-fitted by five curves. The main peak centered at 284.8 eV corresponded to the C–C bonding in graphite and an adsorbed hydrocarbon layer, indicating that some graphitic domains could exist in the nanowalls [40, 41]. In addition, D- and G-modes were observed in Raman spectra of h-BNNWs (see Fig. S2 in the ESM) confirming the incorporation of graphitic domains. The peaks at 286.9, 288.2 and 291.4 eV corresponded to C–N, C–O and C–F bonds, respectively, which were most likely concentrated in the adsorbed hydrocarbon layer [42–44]. The presence of such a layer on the film surfaces is a typical phenomenon that has been described by many authors, and a well-developed surface can significantly enhance it [45, 46]. The shoulder at 282.7 eV was attributed to C–B bonds indicating the doping of carbon atoms in nanowalls [47]. Thus, the presence of C–N and C–B bonding in BNNWs can also demonstrate possible existence of boundaries between the h-BN and graphitic regions. The N1s spectra in Fig. 2(c) can be fitted by two curves: The main one with the binding energy peak centered at 398.3 eV was attributed to the sp^2 B–N bonding [37] and the other one centered at 399.6 eV referred to the C–N bonding [40].

In addition to the binding energies, the energy difference between different XPS peaks is an important parameter. In the presented spectra the difference between B1s and N1s peaks was 207.6 ± 0.2 eV. This value is in a good agreement with the published data for hexagonal boron nitride [37]. Both the B1s and the N1s spectra signified that the sp^2 B–N bonding (as in h-BN) is the main configuration for B and N atoms in the maze-like and wavy h-BN nanowalls. The XPS data also showed that two morphological types of nanowalls differed in the concentration of B–C bonds only. This factor can be critical for the understanding of the origin of the

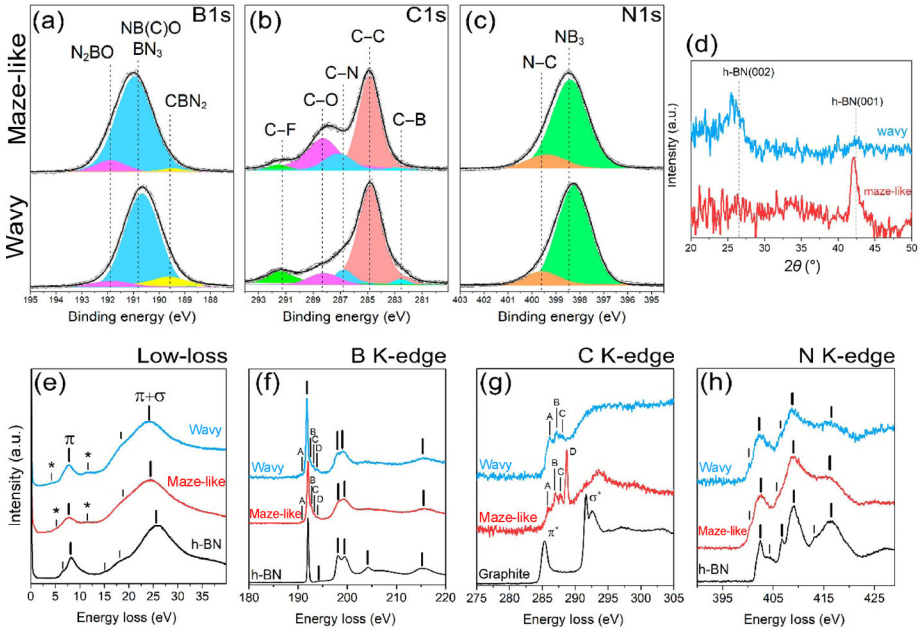

Figure 2 High-resolution (a) B1s, (b) C1s and (c) N1s XPS spectra of the maze-like and wavy h-BN nanowalls demonstrate the presence of carbon- and oxygen-containing bonds in addition to B–N bonding. The maze-like BNNWs contained more carbon atoms and exhibited a texture effect confirmed by XRD analysis. (d) The XRD pattern of maze-like BNNWs contained only (001) peak. (e)–(h) EELS measurements were in agreement with XPS data. (e) Low-loss EEL spectra of BNNWs were similar to h-BN reference. Carbon-doped h-BN nanowalls demonstrated characteristic peaks in (f) B, (g) C and (h) N K-edge EEL spectra.

morphological difference.

To further investigate the bond structure of the BNNWs, EELS measurements were performed. The low-loss EEL spectra of the maze-like and wavy h-BN nanowalls, and of a reference h-BN crystal are presented in Fig. 2(e). The spectra showed π- and π+σ-plasmons at about 7 and 25 eV, respectively. These peaks are typical for sp^2 hybrid system [48]. The low-loss EEL spectra of nanowalls also contained some shoulder structures (indicated by *), which were not observed in the spectrum of h-BN.

Figures 2(f)–2(h) show the B, C and N K-edge EEL spectra of BNNWs. The spectra from reference h-BN and carbon samples are also included for comparison. The B K-edge spectra exhibited one intense and four weak sharp peaks in the π* region between 190–196 eV and a broad structure in the σ* region between 196–205 eV. The intense peak at 192.0 eV corresponded to the characteristic B 1s→π* transition (π* resonance) feature of h-BN, which is a specific fingerprint of sp^2-hybridized B atoms in the hexagonal h-BN network, i.e., a trigonal $B–(N)_3$ bonding environment in h-BN nanowalls [49, 50]. A relatively weak peak at 190.7 eV, marked as A, was attributed to B–C bonding. Low-intensity peaks at 192.5 (B), 193.2 (C) and 193.5 eV (D) corresponded to the oxidized and/or carbonized defects in h-BN nanowalls [51]. The broad feature in the σ* region between 197 and 203 eV was commonly observed in both BNNWs and h-BN samples.

Figure 2(g) compares the C K-edge EEL spectra of h-BN nanowalls with those of the reference graphite. The EEL spectra of nanowalls included three smooth peaks at 284.8 (A), 286.0 (B), and 287.0 (C) eV in the π* region. In case of maze-like nanowalls, additional sharp peak at 288.3 eV was also detected. In the σ* region (290–303 eV), a very broad feature between 294 and 303 eV was observed. The features A, B, and C were associated with the B–C and C–C bonds, respectively, indicating the presence of a very small amount of carbon domains with a graphite-like structure [50, 52]. The presence of the peak at 288.3 eV (labeled as D) was possible due to C–N bonding in the BNNWs structure [50, 52]. However, the peak D can also be classified as contamination signal corresponding to the $C–H_x$ bonding in hydrocarbons [53]. The feature between 294 and 303 eV corresponds to the transitions from the C 1s to the σ* states and to the empty higher-energy states that have p-symmetry components projected onto the carbon sites.

The N K-edge EEL spectra of h-BN nanowalls (Fig. 2(h)) contained three broad peaks and two shoulders. The spectra were similar to those of h-BN indicating the formation of an h-BN-like local structure in BNNWs. The features centered in the range of 400–403 eV, and the relatively broad features centered at 406–417 eV were attributable to π* and σ* resonances, respectively. The π* and σ* features were broader compared with that of h-BN crystal suggesting the presence of various bonding environments [54]. Drawing any conclusion on the bond formation is difficult because peaks that correspond to the N–B and N–C bonds occur very close to each other [50]. However, the π* resonance was almost identical to that of h-BN, which suggests the presence of NB_3 units in the nanowalls. The broad features at about 409 and 416 eV may also be related to the C–N and C=N bonding [55, 56].

3.3 Structural features

The X-ray diffraction (XRD) pattern of the wavy h-BN nanowalls (Fig. 2(d), blue line) contained two broadened XRD peaks with the maximum at 2θ = 25.9° and 42.5° corresponded to the (002) and (100) planes in the hexagonal boron nitride, respectively [57, 58]. On the other hand, the XRD pattern of the maze-like BNNWs (red line) demonstrated single sharp peak at 25.9° indicating preferential orientation of crystallites in contrast to the chaotic distribution in case of the wavy nanowalls.

To investigate the structure and morphology in more detail, cross-sectional TEM images of both maze-like and wavy h-BN nanowalls were taken. The typical TEM image of the nanowalls in Fig. 3 demonstrates that the BNNWs were very thin and almost transparent to the electron beam. The selected area electron diffraction (SAED) patterns (Figs. 3(a) and 3(e)) exhibited three diffraction rings corresponding to 0002, $10\bar{1}0$ and $11\bar{2}0$ of the h-BN structure. Figures 3(a) and 3(e) also show the dark-field TEM images of the two morphological types of BNNWs. In agreement with XRD, the inhomogeneous intensity distribution along the 0002 ring in the SAED pattern and the dark-field TEM image of the maze-like nanowalls clearly indicate the preferential orientation of the h-BN crystallites perpendicularly to the substrate surface. The (002) planes were tilted by the angle of maximum 20° relative to the normal direction of the Si substrate. In case of wavy BNNWs, the SAED pattern demonstrated random orientation and smaller grain size.

High-resolution TEM (HRTEM) images of the BNNWs/substrate interface (Figs. 3(b) and 3(f)) were similar for both morphological types. Amorphous interfacial layer was located between the nanowalls and the substrate. Aligned initially in parallel to the silicon substrate, the h-BN nanosheets have later bent and started vertical growth. The similar structure of interface has been reported for BNNWs fabricated by physical vapor deposition [59] and PECVD [60]. The HRTEM images of the middle of nanowalls in Figs. 3(c) and 3(g)

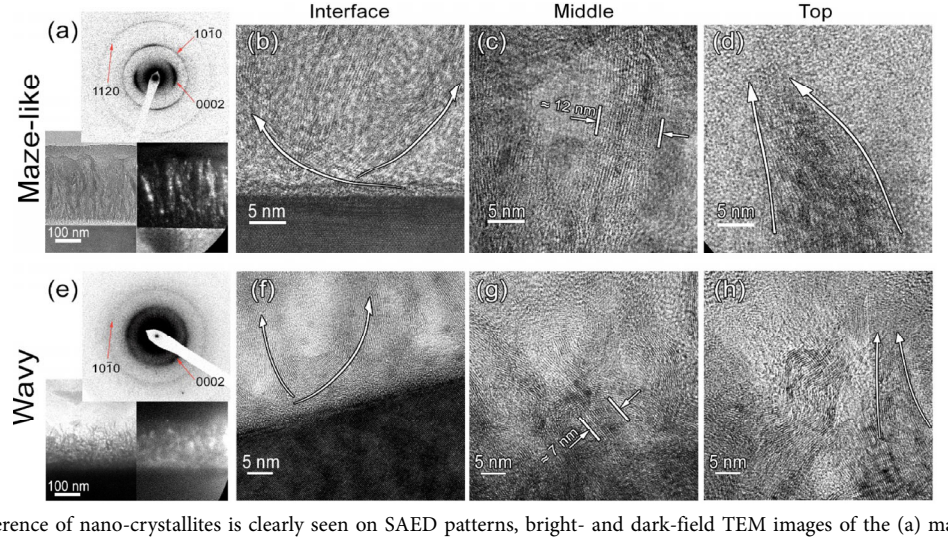

Figure 3 Orientation difference of nano-crystallites is clearly seen on SAED patterns, bright- and dark-field TEM images of the (a) maze-like and (e) wavy h-BN nanowalls. HRTEM images of (b) and (f) interface, (c) and (g) middle and (d) and (h) top of the maze-like and wavy h-BN nanowalls indicated the similarity of crystalline structures. The difference between maze-like and wavy BNNWs is due to the different stacking of nano-crystallites.

show a highly ordered layered lattice. The average spacing between the adjacent fringes was measured to be 0.34 nm that is similar to the d_{002} interplanar distance in h-BN crystal. The thickness of the maze-like and wavy BNNWs was less than 15 and 10 nm, respectively. In addition, the wavy nanowalls were more bending and scrolling. Close to the nanowall edges, the thickness decreased gradually, and the cone-shaped structures were formed leaving many open layers on the surface (Figs. 3(d) and 3(h)). Those open layers are attractive for the applications in hydrogen storage, electron field emission, sensors, and catalyst supports due to their high reaction activity. Cone-shaped structure has been also demonstrated for the wavy h-BN nanowalls obtained by CVD from a mixture of $BF_3 + N_2 + H_2$ [21]. Figures 1(e) and 1(f) illustrate the structure of the maze-like and wavy h-BN nanowalls, respectively.

The h-BN nanowalls with different morphologies were reported to be produced by CVD from various boron-containing precursors such as BF_3, BCl_3, and B [21–23]. However, no one observed the growth of the maze-like BNNWs in these studies. In our work, the maze-like nanowalls were deposited by CVD at the lowest temperature of 400 °C. In addition, two morphological types of h-BN nanowalls were firstly fabricated by one synthesis technique. We found the deposition temperature is critical parameter of morphology transformation. Our previous studies demonstrate that the h-BN nanowalls obtained by PECVD from borazine were structurally similar to the wavy nanowalls but they had the morphology of "maze-like" type [28, 61]. We consider that the low-temperature highly oriented growth of the BNNWs demonstrated in the present study was possible mainly due to the particular chemical properties of the gas system containing organoboron compound and ammonia during PECVD process. It is possible that the carbon atoms contained in precursor molecule were critical for this process.

In summary, the h-BN nanowalls can be divided into different morphological (maze-like and wavy) and structural types (vertically- and randomly-oriented). The "vertically-oriented" h-BN nanowalls should contain vertically-oriented stacks of h-BN nanosheets whereas the "randomly-oriented" nanowalls should contain nanocrystallites without specific orientation. Therefore, the h-BN nanowalls obtained in this study in the range of 400–600 °C were vertically-oriented maze-like BNNWs but randomly-oriented wavy nanowalls could be formed at 700 °C.

3.4 Growth mechanism

Analysis of our experimental data provides an insight into the h-BN nanowall formation leading to a plausible growth mechanism (Fig. 4), which involves several growth stages and helps explain the observed distinctive morphology types at different synthesis temperatures. The growth mechanism is based on aggregated experimental data on h-BN nanowall formation [21, 23, 59] and involves relevant ideas adopted from the growth of carbon nanowalls [62–65].

Usually, during the initial step, a 3–5 nm thick amorphous interfacial layer is formed on the substrate surface (Fig. 4(a)). According to HRTEM and secondary ion mass spectrometry results, the buffer layer is composed of amorphous boron nitride with silicon and oxygen atomic impurities possibly due to a native SiO_x layer formed after chemical treatment [28]. However, the formation of the amorphous layer is not an indispensable prerequisite for vertical h-BN nanosheets growth. For instance, h-BN nanowalls without the interfacial layer have been formed on GaAs(100) [61] and diamond [66]. Then, regions of planar h-BN nanosheets begin to nucleate, as seen in Fig. 4(b). During the second stage, the growth direction changes from parallel to normal (with respect to the substrate) when the growing edges curl upward to release the stress that accumulates when the planar boron nitride domains collide and press upon one another (Fig. 4(c)). The nucleation is likely to be the key mechanism to control the h-BN nanowall morphology. The results of SEM measurements clearly demonstrate the differences in nuclei shape and size of maze-lake and wavy h-BN nanowalls (see Fig. S3 in the ESM). Fewer nuclei of planar h-BN layers per unit area lead to the wide front of h-BN nanosheets colliding with each other. As a result, elongated nuclei of maze-like nanowalls emerge. On the other hand, spherical particles are formed when larger nuclei of planar h-BN layers are present per unit area in the case of wavy nanowalls. In the last step, dissociation of species in the plasma continuously provides the radicals, ions, and neutrals to the vertically growing hexagonal lattice (Fig. 4(d)).

The reaction kinetics controlled by the synthesis temperature strongly affects the shape of h-BN nanowalls. The strong bending of wavy nanowalls is likely caused by the increase of precursor decomposition rate at the higher deposition temperature. Consequently, new h-BN islands nucleate on nanowall lateral surfaces (basal planes) leading to nanowall bending, as sketched in Fig. 4(e).

3.5 Thermal stability

The visual thermal analysis showed heating in dry air from room temperature to 1,000 °C resulted in the cracking of both maze-like and wavy BNNWs, and partial destruction, which started at 600 °C and finished with evaporation at 800 °C. Thermogravimetric analysis of this material is challenging due to a very low weight of BNNWs, but XPS and SEM measurements can provide detailed information on the nanowall oxidation. Figures 5(a) and 5(b) shows SEM images before and after annealing in argon atmosphere (< 0.01% O_2) at the temperature up to 1,100 °C. The maze-like h-BN nanowalls kept initial morphology after the annealing. In case of the wavy nanowalls, the heat treatment resulted in partial destruction with the preservation of the initial basic morphological features.

The survey XPS spectra showed the presence of boron, nitrogen,

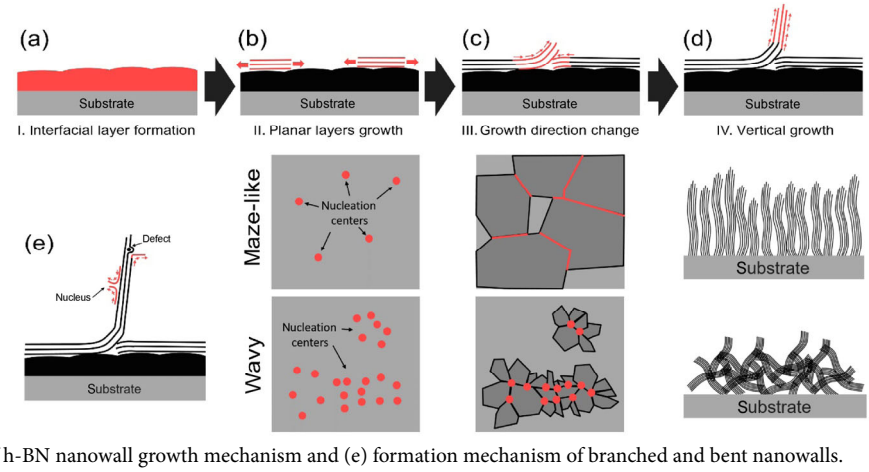

Figure 4 (a)–(d) Schematic of h-BN nanowall growth mechanism and (e) formation mechanism of branched and bent nanowalls.

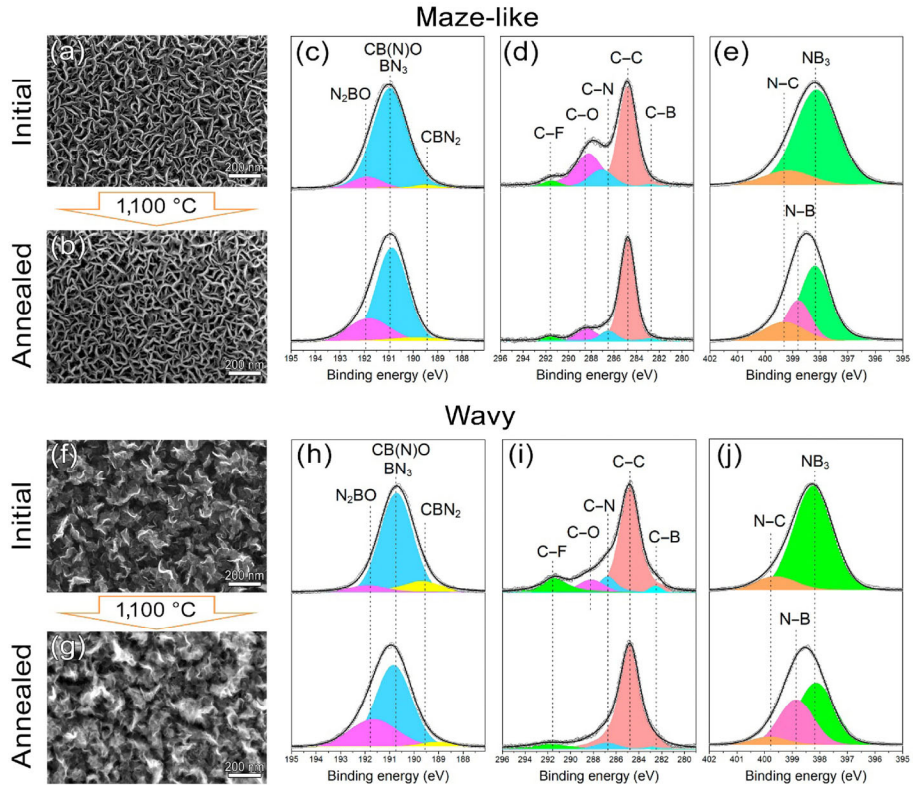

Figure 5 (a) and (b) SEM images demonstrate no changes of the maze-like BNNWs after annealing in inert atmosphere. Insignificant damage of the wavy BNNWs shown on SEM images (f) before and (g) after annealing in inert atmosphere. Oxidation induced the increasing of oxygen-containing peaks were detected in high-resolution B1s, C1s and N1s XPS spectra of the (c)–(e) maze-like and (h)–(j) wavy h-BN nanowalls after annealing.

carbon, oxygen and fluorine atoms in annealed h-BN nanowalls (Fig. S4 in the ESM). F1s photoemission peak corresponds to the surface impurity as described above. Concentration of oxygen atoms increased after annealing due to partial oxidation of the BNNWs (Table 1). Despite very low O_2 concentration in Ar (< 0.01%), the oxygen reacted with h-BN to form the thermodynamically stable B–O bonds. Moreover, the B/N ratio also increased that most probably was caused by the partial changing in the surrounding of the boron atoms.

Figure 5 demonstrates high-resolution C1s, B1s and N1s XPS spectra of BNNWs before and after heat treatment. Similar to the initial samples, the B1s XPS spectra can be fitted by three curves. However, the intensity of the component at 191.8 eV was significantly increased by 23% and 30% for the maze-like and wavy nanowalls, respectively. This peak corresponds to N–B–O bonding and indicates oxidation of nanowalls during annealing [38, 67]. The concentration of B–C bonds decreased for wavy nanowalls, possibly due to the deeper oxidation and reaction between carbon and oxygen atoms. The high-resolution C1s XPS spectra demonstrated lower intensity of all peaks, except for the component at 284.8 eV. This can be attributed to the removal of surface contaminations during annealing. Additional peak at 398.8 eV in the N1s XPS spectra of the annealed samples corresponds to the change in the spatial arrangement of boron and nitrogen atoms due to oxidation [39]. The more intense peaks at 398.8 eV in the N1s spectrum and at 191.8 eV in the B1s spectrum indicate lower oxidation resistivity of the wavy h-BN nanowalls.

Table 1 Elemental composition of BNNWs before and after annealing

Sample		Concentration (at.%)				B/N
		B	N	C	O	
Maze-like	Initial	40.6	38.4	15.8	5.2	1.06
	Annealed	45.8	35.9	9.3	9.0	1.27
Wavy	Initial	42.7	38.8	15.0	3.5	1.10
	Annealed	45.0	36.8	11.8	6.4	1.22

In summary, the highly oriented maze-like h-BN nanowalls possess higher thermal stability in comparison with the randomly oriented wavy nanowalls, although the deposition temperature of the maze-like BNNWs was lower. This difference can likely be related to many defects originated on the bends and edges of nanowalls. In our previous study, we showed that the randomly oriented maze-like h-BN nanowalls synthesized from borazine at 700 °C demonstrated higher thermal stability in comparison with nanowalls obtained at lower temperature [67]. Therefore, the structure of nanowalls is a critical factor for thermal stability and oxidation resistivity.

Present results suggest that the annealing-induced oxidation of BNNWs proceeded in the way described in our previous study [67]. The adsorption of O_2 is followed by a reaction with nitrogen and boron atoms resulting in the oxygen atoms embedment into the h-BN structure with the B–O bonds formation. Formation of an oxidized BN sheet on a low-defected surface of nanowalls can also protect maze-like BNNWs from further reaction with oxygen atoms.

3.6 Luminescence properties

The changes in optical properties of the h-BN nanowalls were studied using the cathodoluminescence (CL) spectroscopy. Figures 6(a) and 6(b) show the room-temperature CL spectra of the samples before and after annealing which demonstrated strong luminescence radiation in the blue-green region. The CL spectra of the maze-like and wavy BNNWs exhibited broad emission band centered at 470 and 540 nm, respectively. Such observations have been attributed to the superimposed effects of deep defect emission and donor–acceptor pair recombination as possibly induced by the presence of carbon and oxygen dopants [68, 69]. In addition, the shift of the luminescence peak of the wavy nanowalls into the higher wavelength region can be related to the presence of the sp^3-structure and size confinement

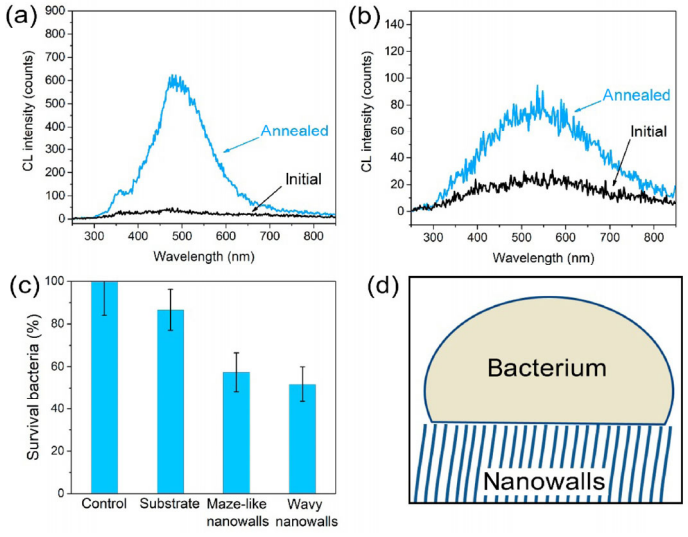

Figure 6 CL spectra of (a) maze-like and (b) wavy BNNWs before and after annealing. Increasing of CL intensity after annealing resulted from the oxygen doping. Cytotoxicity studies reveal potential for BNNWs biomedical applications. (c) Cytotoxicity study showed that h-BN nanowalls demonstrated strong antibacterial effect. (d) Direct contact between nanowalls and bacteria is key for understanding the cytotoxic mechanism. Too low distance between nanowalls can decrease the damage of bacteria cell and cytotoxicity.

[70]. The embedment of additional oxygen atoms in BNNWs resulted in rising of luminescence intensity. However, broadening of wavy nanowalls after heat treatment can negatively affect luminescence. On the other hand, preservation of the initial morphology of the maze-like BNNWs allowed more than 10 times intensification of light emission. Thus, the structural features and the changes in the morphology under oxidation can control and enhance luminescence properties of BNNWs.

3.7 Antibacterial activity

The cytoxicity study of h-BN nanosheets with vertical and random orientation were realized for the first time. We used *E. coli* PQ37 strain as models for Gram-negative bacteria. The Si(100) substrate and the bottom of Petri plate with the area of 10 mm ×10 mm were used as the control and the negative control samples, respectively. Bactericidal activity of the h-BN nanowalls against *E. coli* bacteria is presented in Fig. 6(c). For the control sample, no considerable antibacterial activity was observed in our experimental conditions. However, the BNNWs exhibited considerable antibacterial activities. In fact, after 1 h, 57.4% ± 9.1% and 51.7% ± 8.2% of the bacteria could survive on the surface of the maze-like and of the wavy h-BN nanowalls, respectively.

Over the past few years, many articles on the biocompatibility of h-BN materials have been published. Most important research has highlighted no adverse effects following h-BN nanotubes and nanoparticles administration to several cell lines [30, 71, 72]. Moreover, good results in terms of *in vivo* toxicological investigation have been recently pointed out [73]. However, a comprehensive study by Horvàth et al. displayed a relevant toxicity of h-BN nanotubes tested on several cell lines. The nanoparticle aspect ratio is considered to play a key role in the biocompatibility evaluation [30].

Biocompatibility of carbon nanowalls (structural analogue of BNNWs) was also studied by Ion et.al. [74]. The results demonstrated that osteoblasts adhere and remain long term viable on carbon nanowalls. Moreover, the investigated scaffold cell proliferation was significantly promoted. On the other hand, Akhavan et.al. have reported significant cytotoxic effect of the graphene oxide and reduced graphene oxide nanowalls against both Gram-positive and Gram-negative models of bacteria [75]. Only 41% ± 8% and 16% ± 3% of the bacteria could survive on the surface of the graphene oxide and reduced graphene oxide nanowalls after 1 h, respectively. It was found that the damage of bacteria cell membrane caused by direct contact with extremely sharp edges of the nanowalls was the effective mechanism in the bacterial inactivation. Moreover, the reduced graphene oxide nanowalls were more toxic due to the better charge transfer between the bacteria and the more sharpened edges of the reduced nanowalls during the contact interaction.

We suggest that the cytotoxicity of h-BN nanowalls can also be attributed to the interaction between the sharp edges of the nanowalls with the cell membrane of the bacteria. A lower toxic effect of the maze-like nanowalls can be explained by a higher density of nanowall distribution resulting in decreased damage due to the distribution of mass on many support points like a yogi lying on the bed of nails. Schematic image of the effect is presented in Fig. 6(d). However, cytotoxicity against other bacteria and cells, as also mechanism of antibacterial effect require further studies.

4 Concliusions

We performed a study of structural features, cytotoxicity, thermal stability and luminescence of two morphological types of h-BN nanowalls. The first type—the maze-like nanowalls—was synthesized in the temperature range of 400–600 °C. The temperature of 400 °C is the lowest CVD synthesis temperature for all types of h-BN nanowalls. The deposition temperature of the second type—the wavy nanowalls—was 700 °C. The maze-like BNNWs contained vertically aligned stacks of h-BN nanosheets of less 15 nm in thickness, whereas the wavy nanowalls strongly deformed randomly oriented h-BN nanocrystallites. Morphological type of BNNWs was successfully controlled by the deposition temperature. XPS and EELS measurements showed that h-BN lattice of nanowalls can contain the graphene domains. Despite lower synthesis temperature, thermal stability and oxidation resistivity of the maze-like BNNWs were higher in comparison with the wavy nanowalls. Annealing in argon atmosphere with low amount of O_2 resulted in a replacement of nitrogen atoms in the initial h-BN lattice by oxygen atoms. Oxygen-doped h-BN nanowalls demonstrated enhanced luminescent properties in the blue-green region. The oxygen-doped maze-like BNNWs exhibited stronger increase in the emission intensity. Therefore, the structure of nanowalls was found to be the critical factor for their stability and emitting properties. Significant cytotoxicity of both maze-like and wavy h-BN nanowalls against *E. coli* was demonstrated for the first time. The antibacterial effect may be related to the damage of cell membrane by direct contact of bacteria with the very sharp edges of the nanowalls and requires further studies. The present study opens new insights on structural and morphological features of h-BN nanowalls and demonstrates the potential application of BNNWs in biomedicine and nanoelectronics.

Acknowledgements

The reported research was funded by Russian Foundation for Basic Research and the government of the Novosibirsk region of the Russian Federation (No. 18-43-543003). The project was partially performed in the resource centers of Scientific Park of Saint-Petersburg State University, in particular, Center for X-ray Diffraction Studies, Thermogravimetric and Calorimetric Research Center, Center for Physical Methods of Surface Investigation and Nanotechnology Interdisciplinary Center. K. O. thanks the Australian Research Council for partial support, UrFU for the access to scientific equipment of Laboratory "Nanocrystal" supported by Act 211 Government of the RF (No. 02.A03.21.0006).

Electronic Supplementary Material: Supplementary material (XPS

and Raman spectra, SEM images) is available in the online version of this article at https://doi.org/10.1007/s12274-018-2185-7.

References

[1] Novoselov, K. S.; Geim, A. K.; Morozov, S. V.; Jiang, D.; Zhang, Y.; Dubonos, S. V.; Grigorieva, I. V.; Firsov, A. A. Electric field effect in atomically thin carbon films. *Science* **2004**, *306*, 666–669.

[2] Pakdel, A.; Bando, Y.; Golberg, D. Nano boron nitride flatland. *Chem. Soc. Rev.* **2014**, *43*, 934–959.

[3] Falin, A.; Cai, Q.; Santos, E. J. G.; Scullion, D.; Qian, D.; Zhang, R.; Yang, Z.; Huang, S. M.; Watanabe, K.; Taniguchi, T. et al. Mechanical properties of atomically thin boron nitride and the role of interlayer interactions. *Nat. Commun.* **2017**, *8*, 15815.

[4] Li, L. H.; Cervenka, J.; Watanabe, K.; Taniguchi, T.; Chen, Y. Strong oxidation resistance of atomically thin boron nitride nanosheets. *ACS Nano* **2014**, *8*, 1457–1462.

[5] Haubner, R.; Wilhelm, M.; Weissenbacher, R.; Lux, B. Boron nitrides—Properties, synthesis and applications. In *High Performance Non-Oxide Ceramics. II. Structure and Bonding*; Jansen, M., Ed.; Springer: Berlin, Heidelberg, Germany, 2002; pp 1–45.

[6] Li, L. H.; Chen, Y.; Cheng, B.-M.; Lin, M.-Y.; Chou, S.-L.; Peng, Y.-C. Photoluminescence of boron nitride nanosheets exfoliated by ball milling. *Appl. Phys. Lett.* **2012**, *100*, 261108.

[7] Weng, Q. H.; Wang, X. B.; Wang, X.; Bando, Y.; Golberg, D. Functionalized hexagonal boron nitride nanomaterials: Emerging properties and applications. *Chem. Soc. Rev.* **2016**, *45*, 3989–4012.

[8] Mateti, S.; Wong, C. S.; Liu, Z.; Yang, W. R.; Li, Y. C.; Li, L. H.; Chen, Y. Biocompatibility of boron nitride nanosheets. *Nano Res.* **2018**, *11*, 334–342.

[9] Sun, M. M.; Dong, J. C.; Lv, Y.; Zhao, S. Q.; Meng, C. X.; Song, Y. J.; Wang, G. X.; Li, J. F.; Fu, Q.; Tian, Z. Q. et al. Pt@h-BN core–shell fuel cell electrocatalysts with electrocatalysis confined under outer shells. *Nano Res.* **2018**, *11*, 3490–3498.

[10] Sun, M. M.; Fu, Q.; Gao, L. J.; Zheng, Y. P.; Li, Y. Y.; Chen, M. S.; Bao, X. H. Catalysis under shell: Improved CO oxidation reaction confined in Pt@h-BN core–shell nanoreactors. *Nano Res.* **2017**, *10*, 1403–1412.

[11] Li, L.; Li, L. H.; Ramakrishnan, S.; Dai, X. J.; Nicholas, K.; Chen, Y.; Chen, Z. Q.; Liu, X. W. Controlling wettability of boron nitride nanotube films and improved cell proliferation. *J. Phys. Chem. C* **2012**, *116*, 18334–18339.

[12] Cai, Q. R.; Mateti, S.; Watanabe, K.; Taniguchi, T.; Huang, S. M.; Chen, Y.; Li, L. H. Boron nitride nanosheet-veiled gold nanoparticles for surface-enhanced Raman scattering. *ACS Appl. Mater. Interfaces* **2016**, *8*, 15630–15636.

[13] Cai, Q. R.; Mateti, S.; Yang, W. R.; Jones, R.; Watanabe, K.; Taniguchi, T.; Huang, S. M.; Chen, Y.; Li, L. H. Boron nitride nanosheets improve sensitivity and reusability of surface-enhanced Raman spectroscopy. *Angew. Chem., Int. Ed.* **2016**, *55*, 8405–8409.

[14] Wu, Y. H.; Shen, Z. X.; Yu, T. *Two-Dimensional Carbon: Fundamental Properties, Synthesis, Characterization, and Applications*; CRC Press: Boca Raton, FL, USA, 2014.

[15] Yu, K. H.; Wang, P. X.; Lu, G. H.; Chen, K.-H.; Bo, Z.; Chen, J. H. Patterning vertically oriented graphene sheets for nanodevice applications. *J. Phys. Chem. Lett.* **2011**, *2*, 537–542.

[16] Mao, S.; Yu, K. H.; Chang, J. B.; Steeber, D. A.; Ocola, L. E.; Chen, J. H. Direct growth of vertically-oriented graphene for field-effect transistor biosensor. *Sci. Rep.* **2013**, *3*, 1696.

[17] Ren, G. F.; Pan, X.; Bayne, S.; Fan, Z. Y. Kilohertz ultrafast electrochemical supercapacitors based on perpendicularly-oriented graphene grown inside of nickel foam. *Carbon* **2014**, *71*, 94–101.

[18] Seo, D. H.; Han, Z. J.; Kumar, S.; Ostrikov, K. K. Structure-controlled, vertical graphene-based, binder-free electrodes from plasma-reformed butter enhance supercapacitor performance. *Adv. Energy Mater.* **2013**, *3*, 1316–1323.

[19] Malesevic, A.; Kemps, R.; Vanhulsel, A.; Chowdhury, M. P.; Volodin, A.; Van Haesendonck, C. Field emission from vertically aligned few-layer graphene. *J. Appl. Phys.* **2008**, *104*, 084301.

[20] Wu, Y. H.; Yang, B. J.; Zong, B. Y.; Sun, H.; Shen, Z. X.; Feng, Y. P. Carbon nanowalls and related materials. *J. Mater. Chem.* **2004**, *14*, 469–477.

[21] Yu, J.; Qin, L.; Hao, Y. F.; Kuang, S. Y.; Bai, X. D.; Chong, Y.-M.; Zhang, W. J.; Wang, E. G. Vertically aligned boron nitride nanosheets: Chemical vapor synthesis, ultraviolet light emission, and superhydrophobicity. *ACS Nano* **2010**, *4*, 414–22.

[22] Zhang, C.; Hao, X. P.; Wu, Y. Z.; Du, M. Synthesis of vertically aligned boron nitride nanosheets using CVD method. *Mater. Res. Bull.* **2012**, *47*, 2277–2281.

[23] Pakdel, A.; Zhi, C. Y.; Bando, Y.; Nakayama, T.; Golberg, D. Boron nitride nanosheet coatings with controllable water repellency. *ACS Nano* **2011**, *5*, 6507–6515.

[24] Kesler, V. G.; Kosinova, M. L.; Rumyantsev, Y. M.; Sulyaeva, V. S. X-ray photoelectron and Auger spectroscopic study of the chemical composition of BC_xN_y films. *J. Struct. Chem.* **2012**, *53*, 699–707.

[25] Levy, R. A.; Mastromatteo, E.; Grow, J. M.; Paturi, V.; Kuo, W. P.; Boeglin, H. J.; Shalvoy, R. Low pressure chemical vapor deposition of B-N-C-H films from triethylamine borane complex. *J. Mater. Res.* **1995**, *10*, 320–327.

[26] Choy, K. L. Chemical vapour deposition of coatings. *Prog. Mater. Sci.* **2003**, *48*, 57–170.

[27] Meyyappan, M.; Delzeit, L.; Cassell, A.; Hash, D. Carbon nanotube growth by PECVD: A review. *Plasma Sources Sci. Technol.* **2003**, *12*, 205–216.

[28] Merenkov, I. S.; Kosinova, M. L.; Ermakova, E. N.; Maksimovskii, E. A.; Rumyantsev, Y. M. PECVD synthesis of hexagonal boron nitride nanowalls from a borazine + ammonia mixture. *Inorg. Mater.* **2015**, *51*, 1097–1103.

[29] Boo, J. H.; Rohr, C.; Ho, W. Growth of boron nitride thin films on silicon substrates using new organoboron precursors. *Phys. Stat. Sol. (A)* **1999**, *176*, 705–710.

[30] Ciofani, G.; Del Turco, S.; Rocca, A.; de Vito, G.; Cappello, V.; Yamaguchi, M.; Li, X.; Mazzolai, B.; Basta, G.; Gemmi, M. et al. Cytocompatibility evaluation of gum Arabic-coated ultra-pure boron nitride nanotubes on human cells. *Nanomedicine* **2014**, *9*, 773–788.

[31] Merenkov, I. S.; Kasatkin, I. A.; Maksimovskii, E. A.; Alferova, N. I.; Kosinova, M. L. Vertically aligned layers of hexagonal boron nitride: PECVD synthesis from triethylaminoborane and structural features. *J. Struct. Chem.* **2017**, *58*, 1018–1024.

[32] Sato, Y.; Terauchi, M.; Mukai, M.; Kaneyama, T.; Adachi, K. High energy-resolution electron energy-loss spectroscopy study of the dielectric properties of bulk and nanoparticle LaB_6 in the near-infrared region. *Ultramicroscopy* **2011**, *111*, 1381–1387.

[33] BenMoussa, B.; D'Haen, J.; Borschel, C.; Barjon, J.; Soltani, A.; Mortet, V.; Ronning, C.; D'Olieslaeger, M.; Boyen, H.-G.; Haenen, K. Hexagonal boron nitride nanowalls: Physical vapour deposition, 2D/3D morphology and spectroscopic analysis. *J. Phys. D: Appl. Phys.* **2012**, *45*, 135302.

[34] Yang, C. Y.; Bi, H.; Wan, D. Y.; Huang, F. Q.; Xie, X. M.; Jiang, M. H. Direct PECVD growth of vertically erected graphene walls on dielectric substrates as excellent multifunctional electrodes. *J. Mater. Chem. A* **2013**, *1*, 770–775.

[35] Hiramatsu, M.; Hori, M. Fabrication of carbon nanowalls using novel plasma processing. *Jpn. J. Appl. Phys.* **2006**, *45*, 5522–5527.

[36] Xu, S.; Ma, X.; Su, M. Investigation of BCN films deposited at various hboxN_2/hboxAr flow ratios by DC reactive magnetron sputtering. *IEEE Trans. Plasma Sci.* **2006**, *34*, 1199–1203.

[37] Jeon, J.-K.; Uchimaru, Y.; Kim, D.-P. Synthesis of novel amorphous boron carbonitride ceramics from the borazine derivative copolymer via hydroboration. *Inorg. Chem.* **2004**, *43*, 4796–4798.

[38] Gouin, X.; Grange, P.; Bois, L.; L'Haridon, P.; Laurent, Y. Characterization of the nitridation process of boric acid. *J. Alloys Compd.* **1995**, *224*, 22–28.

[39] Il'inchik, E. A.; Merenkov, I. S. X-ray photoelectron study of the effect of the composition of the initial gas phase on changes in the electronic structure of hexagonal boron nitride films obtained by PECVD from borazine. *J. Struct. Chem.* **2016**, *57*, 670–678.

[40] Liu, L. H.; Wang, Y. X.; Feng, K. C.; Li, Y. G.; Li, W. Q.; Zhao, C. H.; Zhao, Y. N. Preparation of boron carbon nitride thin films by radio frequency magnetron sputtering. *Appl. Surf. Sci.* **2006**, *252*, 4185–4189.

[41] Dinescu, M.; Perrone, A.; Caricato, A. P.; Mirenghi, L.; Gerardi, C.; Ghica, C.; Frunza, L. Boron carbon nitride films deposited by sequential pulses laser deposition. *Appl. Surf. Sci.* **1998**, *127–129*, 692–696.

[42] Wada, Y.; Yap, Y. K.; Yoshimura, M.; Mori, Y.; Sasaki, T. The control of B–N and B–C bonds in BCN films synthesized using pulsed laser deposition. *Diam. Relat. Mater.* **2000**, *9*, 620–624.

[43] Zhou, F.; Adachi, K.; Kato, K. Friction and wear behavior of BCN coatings sliding against ceramic and steel balls in various environments. *Wear* **2006**, *261*, 301–310.

[44] Lei, Y.-G.; Ng, K.-M.; Weng, L.-T.; Chan, C.-M.; Li, L. XPS C 1s binding energies for fluorocarbon-hydrocarbon microblock copolymers. *Surf. Interface Anal.* **2003**, *35*, 852–855.
[45] Guimon, C.; Gonbeau, D.; Pfister-Guillouzo, G.; Dugne, O.; Guette, A.; Naslain, R.; Lahaye, M. XPS study of BN thin films deposited by CVD on SiC plane substrates. *Surf. Interface Anal.* **1990**, *16*, 440–445.
[46] Linss, V.; Rodil, S. E.; Reinke, P.; Garnier, M. G.; Oelhafen, P.; Kreissig, U.; Richter, F. Bonding characteristics of DC magnetron sputtered B–C–N thin films investigated by Fourier-transformed infrared spectroscopy and X-ray photoelectron spectroscopy. *Thin Solid Films* **2004**, *467*, 76–87.
[47] Künzli, H.; Gantenbein, P.; Steiner, R.; Oelhafen, P. Deposition and characterization of thin boron-carbide coatings. *Fresenius J. Anal. Chem.* **1993**, *346*, 41–44.
[48] Huang, J. Y.; Yasuda, H.; Mori, H. HRTEM and EELS studies on the amorphization of hexagonal boron nitride induced by ball milling. *J. Am. Ceram. Soc.* **2000**, *83*, 403–409.
[49] Jiménez, I.; Jankowski, A.; Terminello, L. J.; Carlisle, J. A.; Sutherland, D. G. J.; Doll, G. L.; Mantese, J. V.; Tong, W. M.; Shuh, D. K.; Himpsel, F. J. Near-edge X-ray absorption fine structure study of bonding modifications in BN thin films by ion implantation. *Appl. Phys. Lett.* **1996**, *68*, 2816–2818.
[50] Ray, S. C.; Tsai, H. M.; Chiou, J. W.; Jan, J. C.; Kumar, K.; Pong, W. F.; Chien, F. Z.; Tsai, M.-H.; Chattopadhyay, S.; Chen, L. C. et al. X-ray absorption studies of boron–carbon–nitrogen ($B_xC_yN_z$) ternary alloys. *Diam. Relat. Mater.* **2004**, *13*, 1553–1557.
[51] Caretti, I.; Jiménez, I. Point defects in hexagonal BN, BC_3 and BC_xN compounds studied by X-ray absorption near-edge structure. *J. Appl. Phys.* **2011**, *110*, 023511.
[52] Franke, R.; Bender, S.; Jüngermann, H.; Kroschel, M.; Jansen, M. The determination of structural units in amorphous Si–B–N–C ceramics by means of Si, B, N and C K—XANES spectroscopy. *J. Electron Spectrosc. Relat. Phenom.* **1999**, *101–103*, 641–645.
[53] Stöhr, J. *NEXAFS Spectroscopy*; Springer: Berlin, Heidelberg, Germany, 1992.
[54] Ray, S. C.; Tsai, H. M.; Bao, C. W.; Chiou, J. W.; Jan, J. C.; Kumar, K. P. K.; Pong, W. F.; Tsai, M.-H.; Chattopadhyay, S.; Chen, L. C. et al. Electronic and bonding structures of B-C-N thin films investigated by X-ray absorption and photoemission spectroscopy. *J. Appl. Phys.* **2004**, *96*, 208–211.
[55] Ripalda, J. M.; Román, E.; Díaz, N.; Galán, L.; Montero, I.; Comelli, G.; Baraldi, A.; Lizzit, S.; Goldoni, A.; Paolucci, G. Correlation of X-ray absorption and X-ray photoemission spectroscopies in amorphous carbon nitride. *Phys. Rev. B* **1999**, *60*, R3705–R3708.
[56] Bhattacharyya, S.; Lübbe, M.; Richter, F. Near edge X-ray absorption fine structure of thermally annealed amorphous nitrogenated carbon films. *J. Appl. Phys.* **2000**, *88*, 5043–5049.
[57] Pease, R. S. An X-ray study of boron nitride. *Acta Cryst.* **1952**, *5*, 356–361.
[58] Powder Diffraction Files (PDF) № 34–421. *Powder Diffr. Files № 34–421*.
[59] Hoang, D.-Q.; Pobedinskas, P.; Nicley, S. S.; Turner, S.; Janssens, S. D.; Van Bael, M. K.; D'Haen, J.; Haenen, K. Elucidation of the growth mechanism of sputtered 2D hexagonal boron nitride nanowalls. *Cryst. Growth Des.* **2016**, *16*, 3699–3708.
[60] Merenkov, I. S.; Kasatkin, I. A.; Kosinova, M. L. X-ray diffraction study of vertically aligned layers of h-BN, obtained by PECVD from borazine and ammonia or helium mixtures. *J. Struct. Chem.* **2015**, *56*, 1173–1175.
[61] Merenkov, I. S.; Kosinova, M. L.; Maximovskii, E. A. Boron nitride nanowalls: Low-temperature plasma-enhanced chemical vapor deposition synthesis and optical properties. *Nanotechnology* **2017**, *28*, 185602.
[62] Bo, Z.; Mao, S.; Jun Han, Z.; Cen, K. F.; Chen, J. H.; Ostrikov, K. Emerging energy and environmental applications of vertically-oriented graphenes. *Chem. Soc. Rev.* **2015**, *44*, 2108–2121.
[63] Mironovich, K. V.; Itkis, D. M.; Semenenko, D. A.; Dagesian, S. A.; Yashina, L. V.; Kataev, E. Y.; Mankelevich, Y. A.; Suetin, N. V.; Krivchenko, V. A. Tailoring of the carbon nanowall microstructure by sharp variation of plasma radical composition. *Phys. Chem. Chem. Phys.* **2014**, *16*, 25621–25627.
[64] Zhao, J.; Shaygan, M.; Eckert, J.; Meyyappan, M.; Rümmeli, M. H. A growth mechanism for free-standing vertical graphene. *Nano Lett.* **2014**, *14*, 3064–3071.
[65] Cai, M. Z.; Outlaw, R. A.; Quinlan, R. A.; Premathilake, D.; Butler, S. M.; Miller, J. R. Fast response, vertically oriented graphene nanosheet electric double layer capacitors synthesized from C_2H_2. *ACS Nano* **2014**, *8*, 5873–5882.
[66] Sankaran, K. J.; Hoang, D. Q.; Kunuku, S.; Korneychuk, S.; Turner, S.; Pobedinskas, P.; Drijkoningen, S.; Van Bael, M. K.; D'Haen, J.; Verbeeck, J. et al. Enhanced optoelectronic performances of vertically aligned hexagonal boron nitride nanowalls-nanocrystalline diamond heterostructures. *Sci. Rep.* **2016**, *6*, 29444.
[67] Merenkov, I. S.; Burovihina, A. A.; Zhukov, Y. M.; Kasatkin, I. A.; Medvedev, O. S.; Zvereva, I. A.; Kosinova, M. L. Thermal stability of UV light emitting boron nitride nanowalls. *Mater. Des.* **2017**, *117*, 239–247.
[68] Zhu, Y.-C.; Bando, Y.; Xue, D.-F.; Sekiguchi, T.; Golberg, D.; Xu, F.-F.; Liu, Q.-L. New boron nitride whiskers: Showing strong ultraviolet and visible light luminescence. *J. Phys. Chem. B*. **2004**, *108*, 6193–6196.
[69] Han, W. Q.; Yu, H. G.; Zhi, C. Y.; Wang, J. B.; Liu, Z. X.; Sekiguchi, T.; Bando, Y. Isotope effect on band gap and radiative transitions properties of boron nitride nanotubes. *Nano Lett*. **2008**, *8*, 491–494.
[70] Zhang, H. Z.; Phillips, M. R.; Fitz Gerald, J. D.; Yu, J.; Chen, Y. Patterned growth and cathodoluminescence of conical boron nitride nanorods. *Appl. Phys. Lett.* **2006**, *88*, 093117.
[71] Genchi, G. G.; Ciofani, G. Bioapplications of boron nitride nanotubes. *Nanomedicine* **2015**, *10*, 3315–3319.
[72] Rasel, M. A. I.; Li, T.; Nguyen, T. D.; Singh, S.; Zhou, Y. H.; Xiao, Y.; Gu, Y. T. Biophysical response of living cells to boron nitride nanoparticles: Uptake mechanism and bio-mechanical characterization. *J. Nanopart. Res.* **2015**, *17*, 441.
[73] Soares, D. C. F.; Ferreira, T. H.; de Aguiar Ferreira, C.; Cardoso, V. N.; de Sousa, E. M. B. Boron nitride nanotubes radiolabeled with ^{99m}Tc: Preparation, physicochemical characterization, biodistribution study, and scintigraphic imaging in Swiss mice. *Int. J. Pharm.* **2012**, *423*, 489–495.
[74] Ion, R.; Vizireanu, S.; Luculescu, C.; Cimpean, A.; Dinescu, G. Vertically, interconnected carbon nanowalls as biocompatible scaffolds for osteoblast cells. *J. Phys. D: Appl. Phys.* **2016**, *49*, 274004.
[75] Akhavan, O.; Ghaderi, E. Toxicity of graphene and graphene oxide nanowalls against bacteria. *ACS Nano* **2010**, *4*, 5731–5736.